

Phase diagram of the Hubbard model on a honeycomb lattice: A cluster slave-spin study

Ming-Huan Zeng,¹ Tianxing Ma,^{1,*} and Y.-J. Wang^{1,†}

¹*Department of Physics, Beijing Normal University, Beijing 100875, China*

(Dated: September 24, 2021)

The cluster slave-spin method is implemented to research the ground state properties of the honeycomb lattice Hubbard model with doping δ and coupling U being its parameters. At half-filling, a single direct and continuous phase transition between the semi-metal and antiferromagnetic (AFM) insulator is found at $U_{\text{AFM}} = 2.43t$ that is in the Gross-Neveu-Yukawa universality class, precluding the existence of the intermediate spin liquid state. In the vicinity of this transition, a relation between the staggered magnetization M and the AFM energy gap Δ_{AFM} is established as $M \propto \Delta_{\text{AFM}}$, compared to $M \propto \Delta_{\text{AFM}}(\ln \Delta_{\text{AFM}})^2$ in the square lattice case. For the underlying paramagnetic (PM) state, a first-order semi-metal to insulator Mott transition is corroborated at $U_{\text{Mott}} = 8.36t$, characterized by discontinuities and hystereses, which is responsible for a broad crossover around $U_c = 5.4t$ between the weak- and strong-coupling regimes in the AFM state. In the doped system, unlike the square lattice Hubbard model, this crossover coupling strength U_c increases with doping δ . The compressibility κ near the van Hove singularity at $\delta = 1/4$ is suppressed substantially by the interaction before the semi-metal to AFM transition occurs, whereas κ near the Dirac points is very close to the noninteracting one, indicating that the Dirac cone structure of the energy dispersion is rather robust. Finally, an overall phase diagram in the U - δ plane is presented, which consists of four regimes: the AFM insulator at $\delta = 0$ for $U > U_{\text{AFM}}$, the AFM metal with compressibility $\kappa > 0$ or $\kappa < 0$, and the PM semi-metal, and the AFM metal with $\kappa < 0$ only exists in an extremely small area near the phase boundary between the AFM and PM state and at intermediate coupling strengths.

PACS numbers: 71.27.+a, 71.10.-w, 75.10.Jm

I. INTRODUCTION

The Hubbard Hamiltonian¹ has been acting over decades as a prototypical model for the description of interacting electrons. In spite of its seeming simplicity, this model captures a rich phenomenology of strongly-correlated electrons such as metallic-insulating, nonmagnetic-antiferromagnetic and normal-superconducting phase transitions and can not be solved exactly in more than one dimensions, which necessitates some nonperturbative approaches to deal with the strong-coupling aspect of the model^{2,3}.

In this paper, we will focus on the one-band Hubbard model defined on a honeycomb network, which is bipartite and admits the antiferromagnetism (AFM) in the strong coupling limit. This model has a linear free electron energy dispersion with nodal gapless points at the corners of the Brillouin zone, leading to the so-called Dirac semi-metal. Due to the gapless Dirac points, there is a nontrivial semi-metal to antiferromagnetic insulator (AFMI) transition at a finite coupling strength at half-filling, which makes this model an ideal playground to research the interaction-driven semi-metal to AFMI transition. Up till now, many numerical and analytical methods have been applied to the half-filled system to study this transition and its critical behaviors. Large scale quantum Monte Carlo (QMC) simulations of 648 sites predict a spin liquid state in a range of interaction $3.5t < U < 4.3t$, beyond which the AFM sets in⁴, and this argument was supported by some numerical

works^{5–8}. Nevertheless, this picture was disputed by many other numerical studies^{9–17}, especially those using the same method containing up to 2592 sites^{9,15} and 20808 sites^{16,17}. By means of cluster dynamical mean-field theory, variational cluster approximation, and cluster dynamical impurity approximation, Hassan *et al.*¹⁸ showed that the results are dependent on the shape and size of the clusters, and they claimed that only the system with two bath orbits per cluster boundary site is able to describe the correct behavior and found that the Mott transition for the spin liquid state is actually preempted by the AFM long-range order. Though the early variational cluster calculations¹⁹ argued that the single-particle gap opens at an infinitesimal value of U , recent dynamical cluster approximation study found that this spurious excitation gap is due to the violation of the translation symmetry of the system and the cluster with one bath orbital per cluster site is sufficient for the description of the short-range correlations within the honeycomb unit cell²⁰. Recent study by density matrix embedding theory revealed a paramagnetic insulating state with possible honeycomb cluster state at intermediate coupling strength whose stability is highly cluster and lattice size dependent, and this state is nonexistent in the thermodynamic limit, signaling no intermediate state in the half-filled Hubbard model on a honeycomb lattice²¹. In addition, a two-particle self-consistent study presented a semi-metal to AFMI transition and proved that the transition from a semi-metal to spin liquid phase is forestalled by

this transition²². The functional renormalization group theory predicts a critical interaction strength $U = 3.8t$ that is consistent with the results from the methods mentioned above, supporting that there is no spin liquid state at intermediate coupling strengths^{23,24}.

Based on the charge-spin separation theory^{25–27}, the $U(1)$ slave-spin method has been proposed to cope with the Mott transition in multi-orbital systems²⁸. Then, a cluster slave-spin approach was developed to address strongly correlated systems²⁹ and has been employed to solve the square lattice Hubbard model to obtain an overall ground state phase diagram in the parameter space of doping δ and interaction U ³⁰. In the present work, we apply this method with the Lanczos exact-diagonalization as the cluster solver to the honeycomb lattice Hubbard model to study its ground state properties, including the quantum critical behavior in the vicinity of the interaction-driven semi-metal to AFMI transition at half-filling and an overall phase diagram in the whole U - δ plane. Our motivation is two-fold: (i) Because the results of this model is shown to be highly dependent on the size of the lattice adopted for QMC simulations, as well as the size and shape of the clusters used within various cluster approximations, more results from different approaches ought to be included and compared with each other. (ii) Away from half-filling, much attention was paid to the 1/4-doping, where the free density of states shows a van Hove singularity of logarithmic type, favoring an instability towards superconductivity in the weak interaction regime^{31–33}, whereas an overall U - δ phase diagram pertaining to the magnetism is still absent.

In the honeycomb lattice Hubbard model, we find that the first-order Mott transition occurs at $U_{\text{Mott}} = 8.36t$ in the half-filled PM state, characterized by discontinuities and hystereses in all quantities, and transforms into a broad crossover in the AFM state because of long range AFM correlations. Besides, the phase separation, manifested by a negative compressibility, has been observed in a region near the phase boundary $\delta_M(U)$ between the AFM and PM state and at intermediate couplings, whose area is much smaller compared to the square lattice Hubbard model³⁰. Finally, a phase diagram in the U - δ plane is presented, consisting of four regimes: AFMI, AFM metal with positive and negative compressibility, and the PM semi-metal.

The rest of this paper is organized as follows. In Sec. II, we reintroduce the cluster slave-spin mean-field theory^{29,30} and implement it in the honeycomb lattice Hubbard model by making use of two- and six-site cluster approximations. In Sec. III A, for the half-filled system, an analytical relation between the staggered magnetization M and the AFM energy gap Δ_{AFM} in the vicinity of the semi-metal to AFMI transition is established, and the first-order Mott transition at $U_{\text{Mott}} = 8.36t$ is observed in the PM state. In Sec. III B, the results of finite doping cases obtained by two- and six-site clusters are discussed thoroughly, and we find that

the two-site cluster is inadequate to capture the AFM transition appropriately because it violates the symmetry of the honeycomb lattice. In Sec. IV, the properties of M , Δ_{AFM} , and the compressibility κ are combined to show a phase diagram of the model in the U - δ plane.

II. FORMALISM

The standard one-band fermionic Hubbard model¹ reads

$$H = -t \sum_{\langle i,j \rangle} (c_{i\sigma}^\dagger c_{j\sigma} + \text{H.C.}) + U \sum_i n_{i\uparrow} n_{i\downarrow} - \mu \sum_{i\sigma} n_{i\sigma}, \quad (1)$$

where t , U , μ are the nearest hopping constant, the on-site Coulomb repulsion energy and the chemical potential, respectively. The sum $\langle i,j \rangle$ runs over all pairs of nearest-neighbor sites on a honeycomb lattice, and $c_{i\sigma}^\dagger$ is the creation operator of the electron at site i with spin $\sigma = \uparrow, \downarrow$, and the number operator $n_{i\sigma} = c_{i\sigma}^\dagger c_{i\sigma}$. Hereafter, we use $t = 1$ as the unit of energy.

In the $U(1)$ slave-spin method²⁸, an electron operator is factorized into a slave-spin operator and a fermionic spinon operator

$$c_\alpha^\dagger \equiv S_\alpha^\dagger f_\alpha^\dagger. \quad (2)$$

With the constraint $a_\alpha^\dagger a_\alpha + b_\alpha^\dagger b_\alpha = 1$, the slave-spin operator is rewritten in the Schwinger boson representation

$$S_\alpha^\dagger = a_\alpha^\dagger b_\alpha, \quad S_\alpha^z = \frac{1}{2} (a_\alpha^\dagger a_\alpha - b_\alpha^\dagger b_\alpha). \quad (3)$$

On account of the charge-spin separation (2), the original Hilbert space with basis $\{|0\rangle, |1\rangle\}$ is enlarged to $\{|n_\alpha^f, S_\alpha^z\rangle\} = \{|0, -\frac{1}{2}\rangle, |1, \frac{1}{2}\rangle, |0, \frac{1}{2}\rangle, |1, -\frac{1}{2}\rangle\}$. Thus, an extra constraint needs to be imposed to restrict the Hilbert space to the physical one: $\{|n_\alpha^f, S_\alpha^z\rangle\} = \{|0, -\frac{1}{2}\rangle, |1, \frac{1}{2}\rangle\}$,

$$S_\alpha^z = f_\alpha^\dagger f_\alpha - \frac{1}{2}. \quad (4)$$

To ensure the correct non-interacting behaviors, the slave-boson operators need to be dressed as follows³⁴

$$\tilde{S}_\alpha^\dagger = P_\alpha^\dagger a_\alpha^\dagger b_\alpha P_\alpha, \quad (5a)$$

$$P_\alpha^\pm = \frac{1}{\sqrt{1/2 \pm S_\alpha^z}}. \quad (5b)$$

Following the recipe of Lee and Lee²⁹, with the local constraints (4) being ensured roughly by two global Lagrange multipliers $\lambda_{I\sigma}$ on sublattices $I = A$ and B , Hamiltonian (1) can be cast into the form

$$H_{\text{MF}}^f = -tZ \sum_{\langle i,j \rangle \sigma} (a_{i\sigma}^\dagger b_{j\sigma} + \text{H.C.}) - \sum_{i\sigma} [(\mu + \lambda_{A\sigma} - \tilde{\mu}_{A\sigma}) a_{i\sigma}^\dagger a_{i\sigma} + (\mu + \lambda_{B\sigma} - \tilde{\mu}_{B\sigma}) b_{i\sigma}^\dagger b_{i\sigma}], \quad (6a)$$

$$H_{n_c\text{-site}}^S = H_{n_c\text{-site}}^\lambda + H_{n_c\text{-site}}^U + H_{n_c\text{-site}}^K, \quad (6b)$$

where

$$H_{n_c\text{-site}}^\lambda = \sum_{i_c=1,\sigma}^{n_c} \lambda_{I\sigma} S_{i_c\sigma}^z, \quad (7a)$$

$$H_{n_c\text{-site}}^U = \sum_{i_c=1}^{n_c} U(S_{i_c\sigma}^z + \frac{1}{2})(S_{i_c\bar{\sigma}}^z + \frac{1}{2}), \quad (7b)$$

$$H_{2\text{-site}}^K = \sum_{\sigma} \left\{ \epsilon_{\sigma}^{\delta_1} (\tilde{z}_{A\sigma}^\dagger \tilde{z}_{B\sigma} + \tilde{z}_{B\sigma}^\dagger \tilde{z}_{A\sigma}) + (\epsilon_{\sigma}^{\delta_2} + \epsilon_{\sigma}^{\delta_3}) \right. \\ \left. \times [\tilde{z}_{A\sigma}^\dagger \langle \tilde{z}_{B\sigma} \rangle + \tilde{z}_{B\sigma}^\dagger \langle \tilde{z}_{A\sigma} \rangle + \text{H.C.}] \right\}, \quad (7c)$$

$$H_{6\text{-site}}^K = \sum_{\sigma} \left\{ \epsilon_{\sigma}^{\delta_1} (\tilde{z}_{1\sigma}^\dagger \tilde{z}_{2\sigma} + \tilde{z}_{4\sigma}^\dagger \tilde{z}_{5\sigma}) \right. \\ \left. + \epsilon_{\sigma}^{\delta_2} (\tilde{z}_{1\sigma}^\dagger \tilde{z}_{6\sigma} + \tilde{z}_{3\sigma}^\dagger \tilde{z}_{4\sigma}) + \epsilon_{\sigma}^{\delta_3} (\tilde{z}_{2\sigma}^\dagger \tilde{z}_{3\sigma} + \tilde{z}_{5\sigma}^\dagger \tilde{z}_{6\sigma}) \right. \\ \left. + \epsilon_{\sigma}^{\delta_1} (\tilde{z}_{3\sigma}^\dagger \langle \tilde{z}_{6\sigma} \rangle + \langle \tilde{z}_{3\sigma}^\dagger \rangle \tilde{z}_{6\sigma}) \right. \\ \left. + \epsilon_{\sigma}^{\delta_2} (\tilde{z}_{2\sigma}^\dagger \langle \tilde{z}_{5\sigma} \rangle + \langle \tilde{z}_{2\sigma}^\dagger \rangle \tilde{z}_{5\sigma}) \right. \\ \left. + \epsilon_{\sigma}^{\delta_3} (\tilde{z}_{1\sigma}^\dagger \langle \tilde{z}_{4\sigma} \rangle + \langle \tilde{z}_{1\sigma}^\dagger \rangle \tilde{z}_{4\sigma}) + \text{H.C.} \right\}. \quad (7d)$$

The slave-spin Hamiltonian, describing the electron's charge degrees of freedom, will be treated with n_c -site clusters ($n_c = 2, 6$) marked by the red color geometry in Fig. 1. The cluster will be solved by using the Lanczos exact-diagonalization method. The parameters Z , $\tilde{\mu}_{I\sigma}$, and $\epsilon_{\sigma}^{\delta}$ in Eqs. (6) and (7) are calculated as follows:

$$Z = \langle \tilde{z}_{A\sigma}^\dagger \rangle \langle \tilde{z}_{B\sigma} \rangle, \quad \epsilon_{\sigma}^{\delta_1/2/3} = -t \langle a_{i\sigma}^\dagger b_{i+\hat{\delta}_{1/2/3}\sigma} \rangle, \\ \tilde{\mu}_{I\sigma} = \frac{2Z \langle S_{I\sigma}^z \rangle (\epsilon_{\sigma}^{\delta_1} + \epsilon_{\sigma}^{\delta_2} + \epsilon_{\sigma}^{\delta_3})}{(\frac{1}{2})^2 - \langle S_{I\sigma}^z \rangle^2}. \quad (8)$$

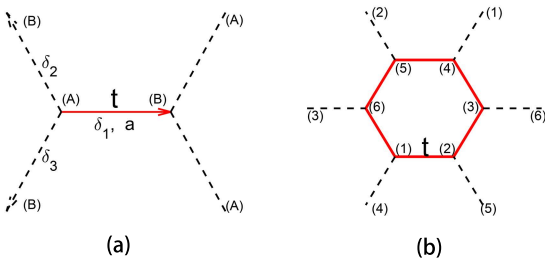


FIG. 1. Schematic illustration of the (a) two- and (b) six-site cluster configurations. The lattice constant a is set to unity, and the positions of three nearest neighbors of site A are $\delta_1 = (1, 0)$, $\delta_2 = (-1/2, \sqrt{3}/2)$, $\delta_3 = -(1/2, \sqrt{3}/2)$.

Moreover, the fermionic spinon Hamiltonian can be Fourier transformed into momentum space:

$$H_{\text{MF}}^f = \sum_{\mathbf{k},\sigma} \left(\varepsilon_{A\sigma} a_{\mathbf{k}\sigma}^\dagger a_{\mathbf{k}\sigma} + \varepsilon_{B\sigma} b_{\mathbf{k}\sigma}^\dagger b_{\mathbf{k}\sigma} \right. \\ \left. + \Gamma_{\mathbf{k}} a_{\mathbf{k}\sigma}^\dagger b_{\mathbf{k}\sigma} + \Gamma_{\mathbf{k}}^* b_{\mathbf{k}\sigma}^\dagger a_{\mathbf{k}\sigma} \right) \quad (9)$$

with

$$\varepsilon_{A/B\sigma} = \tilde{\mu}_{A/B\sigma} - \mu - \lambda_{A/B\sigma}, \\ \Gamma_{\mathbf{k}} = -tZ\gamma_{\mathbf{k}}, \quad \gamma_{\mathbf{k}} = \sum_{\delta} e^{i\mathbf{k}\cdot\delta}. \quad (10)$$

Diagonalization of the spinon Hamiltonian (9) gives rise to the eigenenergies as

$$E_{\mathbf{k}}^{\pm} = \pm \sqrt{|\Gamma_{\mathbf{k}}|^2 + \Delta_{\sigma}^2} - \mu_{\text{eff}}, \quad (11a)$$

$$\mu_{\text{eff}} = \mu - \frac{1}{2}(\tilde{\mu}_{A\sigma} - \lambda_{A\sigma} + \tilde{\mu}_{B\sigma} - \lambda_{B\sigma}), \quad (11b)$$

$$\Delta_{\sigma} = \frac{1}{2}(\tilde{\mu}_{A\sigma} - \lambda_{A\sigma} - \tilde{\mu}_{B\sigma} + \lambda_{B\sigma}). \quad (11c)$$

Here, AFM energy gap $\Delta_{\text{AFM}} = |\Delta_{\sigma}|$ is identical in form to that in the square lattice case^{29,30}.

In most occasions, it proves effective to adopt the density of states (DOS) of the non-interacting electrons to calculate the physical quantities in the thermodynamic limit. On the hexagon lattice, it is defined as

$$D(\gamma) = \frac{1}{N_{\text{triangle}}} \sum_{\mathbf{k}} \delta(\gamma - |\gamma_{\mathbf{k}}|) \\ = \begin{cases} N(\gamma), & (0 \leq \gamma < 1) \\ \tilde{N}(\gamma), & (1 < \gamma \leq 3) \end{cases} \quad (12)$$

where

$$\begin{cases} N(\gamma) = \frac{4}{\pi^2} \frac{\gamma}{\sqrt{(3-\gamma)(1+\gamma)^3}} K\left(\sqrt{\frac{16\gamma}{(3-\gamma)(1+\gamma)^3}}\right), \\ \tilde{N}(\gamma) = \frac{1}{\pi^2} \sqrt{\gamma} K\left(\sqrt{\frac{(3-\gamma)(1+\gamma)^3}{16\gamma}}\right), \end{cases} \quad (13)$$

with $K(x)$ being the first kind complete elliptical integral. In comparison to the self-dual situation on a square lattice, we now have a duality transformation

$$\tilde{\gamma} = \frac{3-\gamma}{1+\gamma} \quad (14)$$

to connect these two parts, under which

$$\frac{(3-\tilde{\gamma})(1+\tilde{\gamma})^3}{16\tilde{\gamma}} = \frac{16\gamma}{(3-\gamma)(1+\gamma)^3}, \quad (15a)$$

$$\frac{(3-\tilde{\gamma})(1+\tilde{\gamma})}{4\tilde{\gamma}} = \frac{4\gamma}{(3-\gamma)(1+\gamma)}, \quad (15b)$$

and

$$\tilde{N}(\gamma) = \frac{(3-\tilde{\gamma})(1+\tilde{\gamma})}{4\tilde{\gamma}} N(\tilde{\gamma}) \\ = \frac{4\gamma}{(3-\gamma)(1+\gamma)} N\left(\frac{3-\gamma}{1+\gamma}\right). \quad (16)$$

Then, the self-consistent quantities $\epsilon_{\sigma}^{\delta} = \epsilon$ and $n_{(A/B)\sigma} \equiv \langle a_{i\sigma}^\dagger a_{i\sigma} \rangle / \langle b_{i\sigma}^\dagger b_{i\sigma} \rangle$ can be calculated through

$$\epsilon = \int_0^3 d\gamma D(\gamma) \frac{(tZ\gamma)^2}{6Z\sqrt{(tZ\gamma)^2 + \Delta^2}} \\ \times \left\{ \theta[-E^+(\gamma)] - \theta[-E^-(\gamma)] \right\}, \quad (17)$$

$$n_{(A/B)\sigma} = \int_0^3 d\gamma D(\gamma) \left[\frac{1}{2} \left(1 \pm \frac{\Delta_\sigma}{\sqrt{(tZ\gamma)^2 + \Delta^2}} \right) \theta(-E_\gamma^+) + \frac{1}{2} \left(1 \mp \frac{\Delta_\sigma}{\sqrt{(tZ\gamma)^2 + \Delta^2}} \right) \theta(-E_\gamma^-) \right], \quad (18)$$

where $E^\pm(\gamma) = \pm\sqrt{(tZ\gamma)^2 + \Delta^2} - \mu_{\text{eff}}$ and $\Delta_\sigma^2 = \Delta^2$.

III. RESULTS AND DISCUSSIONS

A. HALF-FILLED SYSTEM

In this case, the particle-hole symmetry implies $\mu^{\text{eff}} = 0$ and $E^+(\gamma) > 0$, and Eqs. (17) and (18) are simply

$$\begin{aligned} \epsilon &= -\frac{t\lambda}{6} \int_0^3 d\gamma D(\gamma) \frac{\gamma^2}{\sqrt{(\gamma\lambda)^2 + 1}} \\ &= -\frac{t\lambda}{6} I_\epsilon(\lambda), \end{aligned} \quad (19)$$

$$\begin{aligned} \langle S_{(A/B)\sigma}^z \rangle &= (-/+) \frac{\text{sgn}(\Delta_\sigma)}{2} \int_0^3 d\gamma D(\gamma) \frac{1}{\sqrt{(\gamma\lambda)^2 + 1}} \\ &= (-/+) \frac{\text{sgn}(\Delta_\sigma)}{2} I_S(\lambda), \end{aligned} \quad (20)$$

where $\lambda = tZ/\Delta_{\text{AFM}}$ and, by relation (4), $\langle S_{(A/B)\sigma}^z \rangle = n_{(A/B)\sigma} - \frac{1}{2}$.

For the half-filled square lattice Hubbard model at $T = 0$, the AFM order emerges for any nonzero U because of the perfect nesting of the free Fermi surface, whereas the honeycomb lattice is known to have a semi-metal phase at small U due to the low coordination number which allows more fluctuations and an antiferromagnetic phase at large U . It is well established that there is a single direct and continuous phase transition from semi-metal to AFMI at a finite critical interaction strength U_{AFM} for the half-filled honeycomb lattice Hubbard model. This U_{AFM} from large-scale QMC simulations mainly locates around $U \approx 3.8$ ^{9–11,15,17,35}, whereas the results from various cluster scenarios, such as cluster dynamical impurity approximation, variational cluster approximation, dynamical cluster approximation and density matrix embedding theory, are strongly cluster dependent and the U_{AFM} 's are in a wide range of $1.5 \lesssim U \lesssim 4.0$ ^{13,18,19,21,36}. As shown in Fig. 2, we find that $U_{\text{AFM}} = 2.8$ or 2.43 in our two- or six-site cluster approximation, which is larger than that from the Hartree-Fock approximation of 2.235 ^{10,14}, but smaller than those from QMC simulations^{9,11,15,17,35}, reflecting the fact that fluctuations have been incorporated in the six-site cluster, but not enough to give the accurate value. This shortcoming may be remedied by enlarging the cluster size and strictly dealing with the constraint $S_\alpha^z = f_\alpha^\dagger f_\alpha - \frac{1}{2}$ locally. However, the two-site cluster value of U_{AFM} is larger than that from the six-site, necessitating more investigations on the dependence of U_{AFM} upon the cluster size. To extract the critical information around U_{AFM} , we fit our self-consistent data from the six-site

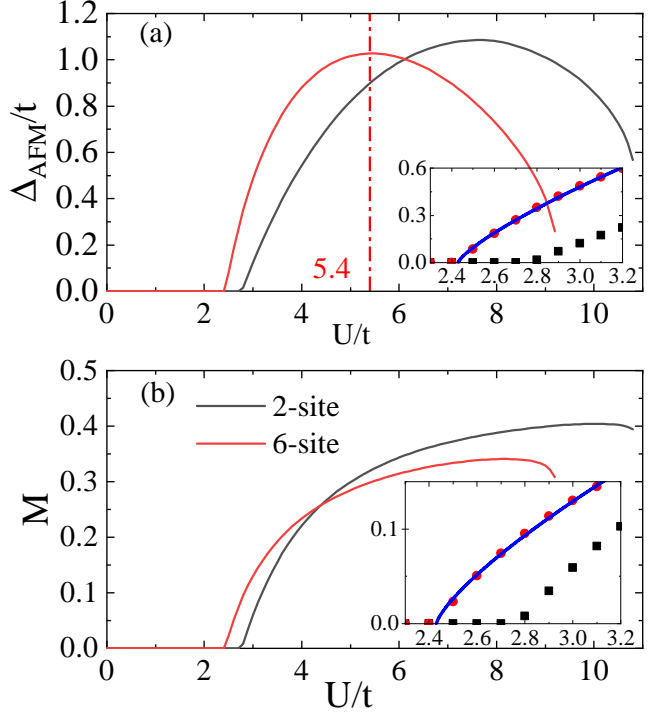


FIG. 2. (a) The AFM energy gap Δ_{AFM} and (b) the staggered magnetization M as function of U , where the insets show the same data in the vicinity of the critical coupling together with the fitting data (blue lines). The results from two-site cluster approximation are presented as well (black).

cluster using the U dependent form of M and Δ_{AFM} that have been verified by QMC simulations^{9,11,15,17} and density matrix embedding theory²¹

$$\Delta_{\text{AFM}}/M = \alpha_{1/2}|U - U_{\text{AFM}}|^{\beta_{1/2}}, \quad (21)$$

and we obtain

$$\begin{cases} \alpha_1 = 0.74021 \pm 0.00836, & \beta_1 = 0.77086 \pm 0.01597; \\ \alpha_2 = 0.19739 \pm 0.000753, & \beta_2 = 0.755 \pm 0.0049. \end{cases} \quad (22)$$

The critical exponent $\beta_2 = 0.755 \pm 0.0049$ for M is very close to those from the large-scale QMC simulations $\beta_2 = 0.75 \pm 0.06$ ⁹ and 0.79 ¹¹, and the critical exponent for single particle gap Δ_{AFM} is slightly larger than that of M ^{11,17}.

We now expand asymptotically the integrals $I_\epsilon(\lambda)$ and $I_S(\lambda)$ defined in Eqs. (19) and (20) as $\lambda \rightarrow \infty$ ³⁷:

$$\epsilon = -\frac{t}{6} \left(1.574597 - 0.448221 \tilde{\Delta}^2 + \frac{4}{3\sqrt{3}\pi} \tilde{\Delta}^3 + \dots \right), \quad (23)$$

$$\begin{aligned} \langle S_{(A/B)\sigma}^z \rangle &= (-/+) \frac{\text{sgn}(\Delta_\sigma)}{2} \left(0.896441 \tilde{\Delta} - \frac{2}{\sqrt{3}\pi} \tilde{\Delta}^2 \right. \\ &\quad \left. - 0.014 \tilde{\Delta}^3 + \frac{4}{9\sqrt{3}\pi} \tilde{\Delta}^4 + \dots \right), \end{aligned} \quad (24)$$

where $\tilde{\Delta} = \lambda^{-1} = \Delta_{\text{AFM}}/tZ$. The relation between M and Δ_{AFM} in the honeycomb lattice around $U = U_{\text{AFM}}$

is established as

$$\begin{aligned} M &= \frac{1}{2} |\langle S_{A\sigma}^z \rangle - \langle S_{B\sigma}^z \rangle| \\ &\approx \frac{1}{2} \left(0.896441 \tilde{\Delta} - \frac{2}{\sqrt{3}\pi} \tilde{\Delta}^2 - 0.014 \tilde{\Delta}^3 + \frac{4}{9\sqrt{3}\pi} \tilde{\Delta}^4 \right). \end{aligned} \quad (25)$$

To the leading order, $M \propto \Delta_{\text{AFM}}$, compared to $M \propto \Delta_{\text{AFM}}(\ln \Delta_{\text{AFM}})^2$ in the square lattice, supporting the AFM at small U in the latter case is driven by the perfect nesting of its free Fermi surface.

On the other hand, Δ_{AFM} reaches its maximum around the crossover coupling strength $U_c = 5.4$ that separates the weak- and strong-coupling regimes, which is consistent with the traditional mean-field behavior $\Delta_{\text{AFM}} \sim U$ at small U , and $\Delta_{\text{AFM}} \sim 4t^2/U$ in the large U limit supported by the super-exchange mechanism. It ought to be mentioned that M drops abruptly when U is larger than a certain value where the quasi-particle weight happens to drop to zero as shown in Fig. 3(a), which may imply that the cluster slave-spin method breaks down for the half-filled system in the large U limit.

The quasi-particle residue Z , the generalized Gutzwiller factor g_t ^{29,38,39}, the holon-doublon correlators C_{ij} ²⁹ between the nearest neighbors C_{12} , the next-nearest neighbors C_{13} and the next-next-nearest neighbors C_{14} , the ground state energy of the slave-spin Hamiltonian per site $\langle H_{n_c\text{-site}}^S \rangle/n_c$ with n_c being the cluster size, and the double occupancy $\langle D \rangle$ as function of U at half-filling obtained from two- and six-site cluster approximations are presented in Fig. 3, where C_{ij} is defined as

$$C_{ij} = \frac{\langle N_i D_j \rangle - \langle N_i \rangle \langle D_j \rangle}{\langle N_i \rangle \langle D_j \rangle} \quad (26)$$

with the holon operator $N_i = (1 - n_{i\sigma})(1 - n_{i\bar{\sigma}})$ and doublon operator $D_j = n_{j\sigma}n_{j\bar{\sigma}}$.

The results are as follows: (i) All quantities in the PM state show discontinuities and hystereses at the critical coupling strength $U_{\text{Mott}} = 8.36$ for the semi-metal to paramagnetic insulator transition as the characteristics of the first-order Mott transition in the PM state^{18,40}. (ii) In Fig. 3(a), compared to that in the PM state, Z is largely suppressed as entering the AFM phase. (iii) In Fig. 3(b)–(d), C_{12} and C_{13} are positive and increase monotonically with U , signaling that the holon and doublon between the nearest and next-nearest neighbors tend to attract each other, and this tendency is enhanced by the coupling strength. However, C_{14} presents a minimum beyond the AFM transition or as U approaches U_{Mott} in the PM state. On the other hand, C_{14} is positive at small and large U while negative for intermediate interaction strengths, suggesting that at half-filling, the holon and doublon between the next-next-nearest neighbors attract each other when U is small or large, while behave repulsively at intermediate U . (iv) In Fig. 3(e), $\langle H_{n_c\text{-site}}^S \rangle/n_c$ in the AFM state is smaller than that from the PM state, favoring an AFM ground state.

(v) In Fig. 3(f), $\langle D \rangle$ in the PM state decreases linearly with increasing U when $U \ll U_{\text{Mott}}$ ⁴¹, whereas in the AFM state, its slope changes abruptly as AFM sets in denoting a second-order transition from a semi-metal to an AFMI. The double occupancy in the AFM state is smaller than that in the PM state when $U_{\text{AFM}} < U \lesssim U_{\text{Mott}}$ or the opposite is true when $U \gtrsim U_{\text{Mott}}$.

B. SYSTEMS WITH FINITE DOPING

In Fig. 4, we plot Z , g_t , Δ_{AFM} , M , $C_{12/3/4}$, $\langle H_{n_c\text{-site}}^S \rangle/n_c$, $\langle D \rangle$ as function of U at $\delta = 0.02$ obtained from two- and six-site cluster approximations. In Fig. 4(a), the quasi-particle residue from six-site cluster is much smaller than that from two-site because of more quantum fluctuations, and becomes flattened when $U > U_{\text{Mott}}$. In Fig. 4(b), the critical coupling strength for AFM transition from six-site cluster is $U_{\text{AFM}} = 3.0$, while that from two-site locates at $U_{\text{AFM}} = 25.0$, which indicates that two-site cluster is inadequate to describe the AFM transition in the honeycomb lattice because it keeps no track of the lattice symmetry. Moreover, in six-site cluster, the coupling strength for the crossover from weak to strong shifts from $U_c = 5.4$ at half-filling to $U_c = 5.8$ at $\delta = 0.02$. In Fig. 4(d), C_{12} increases slowly when $U < U_{\text{Mott}}$, then rises dramatically as U approaches U_{Mott} , and finally grows progressively as U goes to infinity; while C_{13} shows a maximum near U_{Mott} , and the reason is that the hopping probability between the next-nearest neighbors falls faster than the one between the nearest neighbors when U is increased as demonstrated in our previous work on a square lattice³⁰. Unlike C_{12} and C_{13} , both are positive for all U 's, C_{14} is negative at $\delta = 0.02$ and its magnitude grows monotonically with the coupling strength, indicating that the holon and doublon between the next-next-nearest neighbors repulse each other, and this tendency is strengthened as U increases. The negativity of C_{14} can be understood as follows: according to our previous work³⁰, $\langle N_1 D_4 \rangle$ is connected to the hopping probability between site 1 and 4 that decreases dramatically with the growth of U and δ , i.e., in comparison to $\langle N_1 D_4 \rangle > \langle N_1 \rangle \langle D_4 \rangle$ at half-filling, $\langle N_1 D_4 \rangle < \langle N_1 \rangle \langle D_4 \rangle$ at $\delta = 0.02$ and their difference will be widened by the increase of the coupling strength. In Fig. 4(e), as shown by the blue line with $0 < U < 25$ (where the system within two-site approximation is in the PM state.) and the black line, the difference of $\langle H_{n_c\text{-site}}^S \rangle/n_c$ in PM state between two- and six-site cluster approximations is much smaller when $U > U_{\text{Mott}}$, denoting that the cluster size's effect on the properties of the system in the PM state is less important at large U as the system becomes more localized and the inter-site correlations are much weaker in contrast to the weak-coupling limit. In Fig. 4(f), there exists an inflection in $\langle D \rangle$ in the PM state around $U \approx 10$, meaning the first-order Mott transition in the half-filled system turns into a continuous crossover at finite dopings.

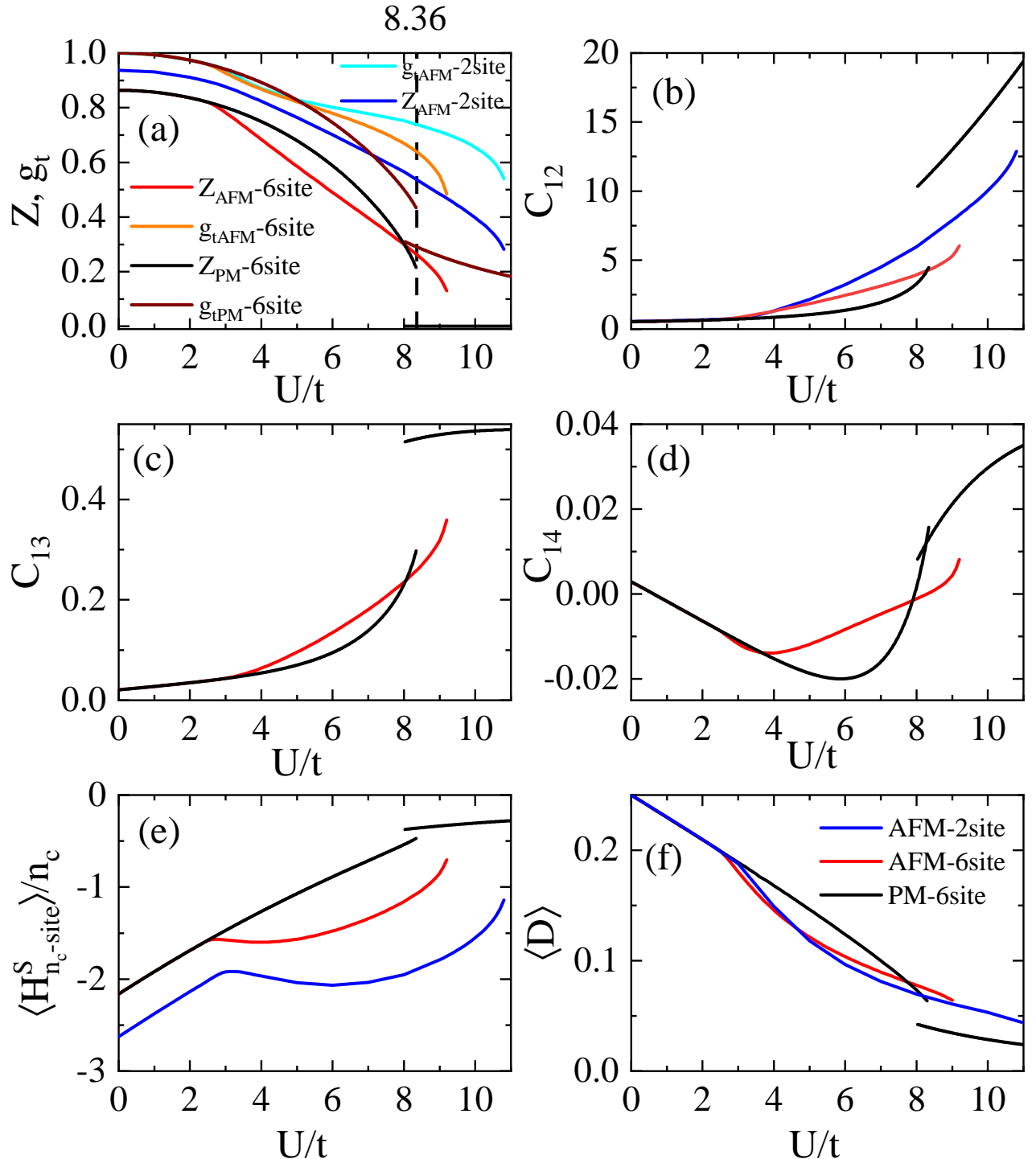


FIG. 3. (a) The quasiparticle weight Z and the generalized Gutzwiller factor g_t . (b)–(d) The holon-doublon correlators between the nearest neighbors C_{12} , the next-nearest neighbors C_{13} and the next-next-nearest neighbors C_{14} . (e) The expectation value of the cluster slave-spin Hamiltonian $\langle H_{n_c\text{-site}}^S \rangle / n_c$. (f) The double occupancy $\langle D \rangle$ in the AFM state vs. U obtained by the 2/6-site clusters (blue/red). All quantities in the PM state obtained by 6-site cluster are black lines.

For $U < 8.0$, the double occupancy in the AFM state is smaller than that in the PM state while the opposite is true for $U > 8.0$, bespeaking that the AFM at small U is triggered by the interaction potential gain while that

in the large U limit is not driven by this mechanism. This picture can also be seen in Fig. 5, where exists a region ($5.4 < U < 8.0$) with $\Delta E_U^{(S)} < 0$ and $\Delta E_K^{(S)} < 0$, signaling that the AFM in this region is supported by

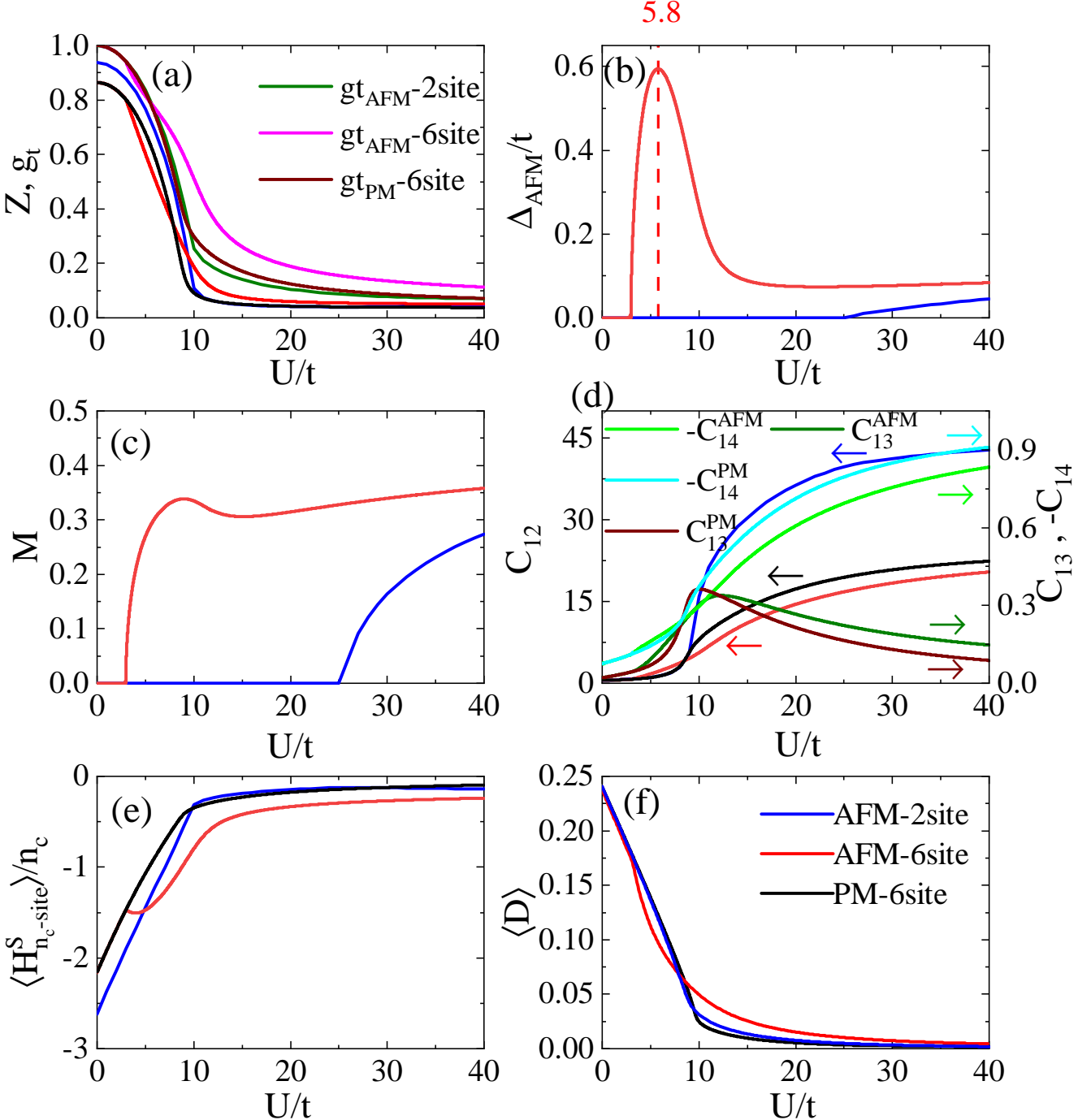


FIG. 4. (a) The quasi-particle weight Z and the generalized Gutzwiller factor g_t , (b) the AFM energy gap Δ_{AFM}/t , (c) the staggered magnetization M , (d) the holon-doublon correlators between the nearest neighbors C_{12} , the next-nearest neighbors C_{13} and the next-next-nearest neighbors C_{14} , (e) the expectation value of the cluster slave-spin Hamiltonian $\langle H_{n_c\text{-site}}^S \rangle/n_c$, and (f) the double occupancy $\langle D \rangle$ as function of U at $\delta = 0.02$ in the AFM state obtained by the two-site (blue) and six-site (red) cluster, as well as the PM state (black) by six-site cluster.

both the kinetic energy and interaction potential gain.

The dependence of the quantities discussed above upon the interaction strength at various dopings of $\delta = 0.02, 0.0375, 0.1, 0.1531, 0.1725$ obtained through six-site cluster approximation are presented in Fig. 6,

where $\delta = 0.1531$ is the critical doping for the AFM to PM phase transition at $U = 40$, and $\delta = 0.1725$ is the maximum of δ_M , i.e., the boundary between the AFM and PM state [see Figs. 8 and 11]. The following results are concluded: (i) In Fig. 6(a), apart

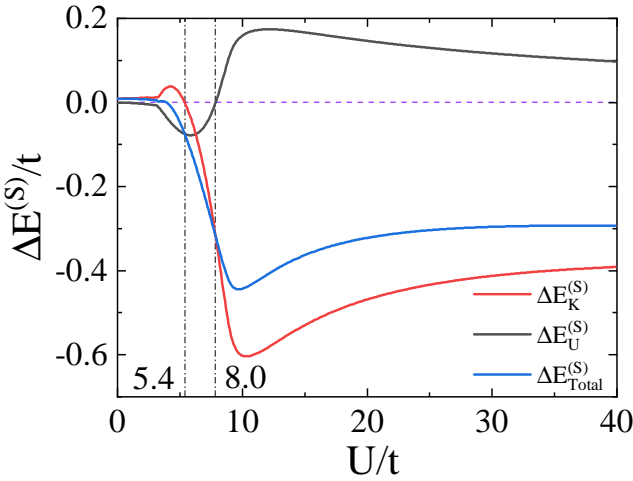


FIG. 5. The difference of the kinetic energy $\Delta E_K^{(S)}$ (red), interaction potential $\Delta E_U^{(S)}$ (black), and their summation $\Delta E_{\text{Total}}^{(S)}$ (blue) of the six-site cluster slave-spin Hamiltonian Eq. (7d) between the AFM and PM states as function of U at $\delta = 0.02$.

from its monotonous diminishing with the growing U at all dopings, Z increases with δ for all coupling strengths, suggesting that the system with the increasing doping tends to be metallic. When $U > U_{\text{Mott}}$, the quasi-particle residues tend approximately to constants, manifesting that the properties in the AFM state are controlled by the underlying Mott transition of the half-filled PM state. (ii) In Fig. 6(b), Δ_{AFM} 's at all dopings exhibit a maximum around the crossover coupling strength $U_c(\delta)$ that grows with δ . Moreover, Δ_{AFM} decreases with increasing δ when $U < U_c(\delta)$, while displays a nonmonotonic behavior for $U > U_c(\delta)$. Interestingly, Δ_{AFM} diminishes to zero as U increases at large dopings, e.g., $\delta = 0.1531, 0.1725$, and this property has also been found in the square lattice Hubbard model^{30,42}. The reason is that the AFM is mostly itinerant when δ approaches the critical dopings δ_M at which the AFM state transits to PM state, and the itinerant AFM is not favored by the overly enhanced localization for large U . (iii) In Fig. 6(c), the staggered magnetization M also rises rapidly, but as δ approaches δ_M , it declines gradually to zero with the increasing U , same as the situation in Δ_{AFM} . (iv) In Fig. 6(d)–(f), C_{12} increases monotonically with U at all dopings and diminishes as δ goes up, which makes it eligible to be an indicator of the magnitude of correlations. There exists a maximum for C_{13} around U_{Mott} , which has been identified as one of features characterizing the strong correlations³⁰. However, C_{14} 's are negative for nonzero dopings, suggesting that the holon and doublon repulse each other when $\delta > 0$, and its magnitude increases with either U or δ . (v) In Fig. 6(g), compared to the PM state, $\langle H_{6\text{-site}}^S \rangle / 6$ is suppressed dramatically as soon as AFM sets in and this effect is weakened by the increasing δ . Moreover, this quantity grows monotonically with δ when $U < U_{\text{Mott}}$ while

displays a nonmonotonic behavior when $U > U_{\text{Mott}}$. (vi) In Fig. 6(h), $\langle D \rangle$ decreases with U and tends to zero as U goes to infinity. Interestingly, this quantity at small U 's diminishes with the increase of δ , while behaves nonmonotonically at large U , reflected by the intersection of the red and blue lines.

The compressibility of the system is defined as $\kappa = n^{-2} \partial n / \partial \mu$. At $U = 0$, it is calculated by using the non-interacting DOS $D(\gamma)$, Eq. (12), via

$$\kappa(\mu) = \begin{cases} \frac{N(|\mu|)}{[\frac{3}{4} + \int_{-\mu}^{\mu} N(|\gamma|) d\gamma]^2}, & (0 < \delta < \frac{1}{4}) \\ \frac{\bar{N}(|\mu|)}{[\int_{-\mu}^{\mu} \bar{N}(|\gamma|) d\gamma]^2}, & (\frac{1}{4} < \delta < 1) \end{cases} \quad (27)$$

which is proportional to the free DOS. For $U > 0$, κ should evolve simultaneously with the quasi-particle DOS which makes it adequate to indicate the dependence of this quantity upon interaction. To illustrate the δ -dependence of the compressibility at various couplings, we plot κ as function of δ at $U = 0, 2, 4, 6$, and 8 in Fig. 7. For $U < U_{\text{AFM}}$, the compressibility near van Hove singularity is suppressed most drastically by interaction, while that at low energy (near the Dirac points) remains very close to the non-interacting one, reflecting that the Dirac cone structure is very robust, and the DOS of the quasi-particles is transferred away from the van Hove singularity as U increases. Furthermore, at $U = 4, 6$, there exhibit a discontinuity at $\delta = \delta_M$ where the AFM-to-PM phase transition occurs, and the one-sided peak of κ as δ approaches δ_M manifests that the system now is an itinerant AFM metal. However, at $U = 8$, there exist two consecutive discontinuities: (i) between positively and negatively divergent κ ; (ii) between negatively divergent and positive small κ .

IV. PHASE DIAGRAM

The staggered magnetization M with U and δ being its parameters is plotted in Fig. 8, where the phase boundary between the AFM and PM states is delineated by $\delta_M(U)$. Obviously, M maximizes at small dopings and large couplings. The phase boundary $\delta_M(U)$ shows a nonmonotonic behavior upon U that may be connected to the crossover of Δ_{AFM} as U increases. We also notice that M saturates when $U > U_{\text{Mott}}$ at small dopings, reflecting that the physical properties in the AFM state are dominated by the underlying Mott transition in the half-filled PM state.

The AFM energy gap Δ_{AFM} in the same parameter space is plotted in Fig. 9, where the phase boundary $\delta_M(U)$ still holds, denoting that there is a single direct and continuous phase transition from a PM semi-metal to an antiferromagnet. The phase transition is in the Gross-Neveu-Yukawa universality class, Eq. (21). An overall crossover between the weak- and strong-coupling regimes can be observed in Δ_{AFM} when U grows, at which Δ_{AFM} reaches its maximum, and the coupling U_c for this crossover is highly δ -dependent, in contrast

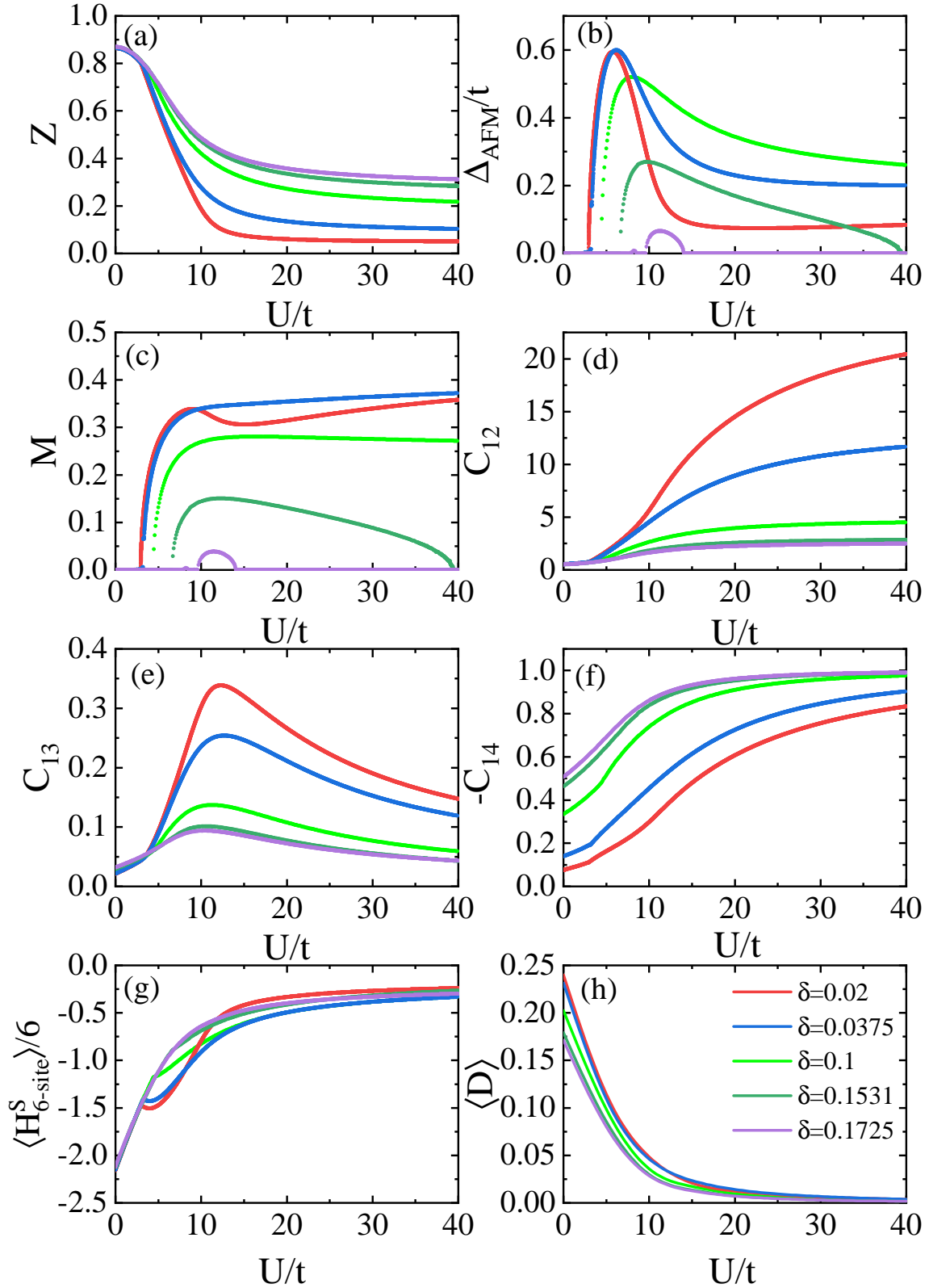


FIG. 6. (a) The quasiparticle weight Z , (b) the AFM energy gap Δ_{AFM}/t , (c) the staggered magnetization M , (d)–(f) the holon-doublon correlator between the nearest neighbors C_{12} , the next-nearest neighbors C_{13} and the next-next-nearest neighbors C_{14} , (g) the expectation value of the cluster slave-spin Hamiltonian, and (h) the double occupancy $\langle D \rangle$ as function of U at a series of doping concentrations $\delta = 0.02$ (red), 0.0375 (blue), 0.1 (green), 0.1531 (dark green), 0.1725 (violet) in the AFM state obtained by the six-site cluster.

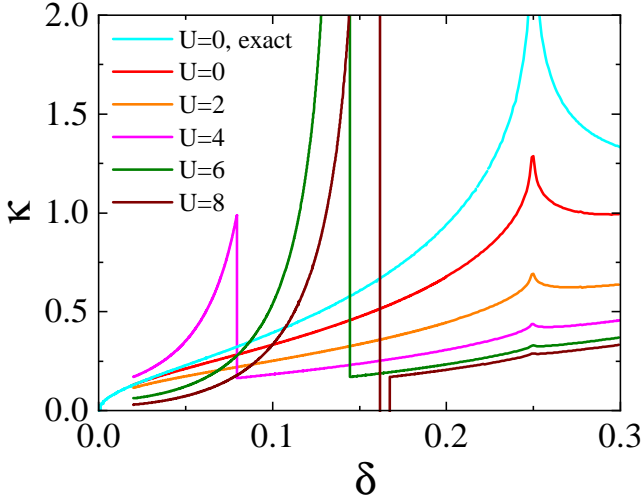


FIG. 7. The compressibility κ obtained from the six-site cluster approximation as function of δ at $U = 0, 2, 4, 6, 8$ (red, orange, magenta, olive, brown, respectively), and the exact one at $U = 0$ calculated through Eq. (27) (cyan).

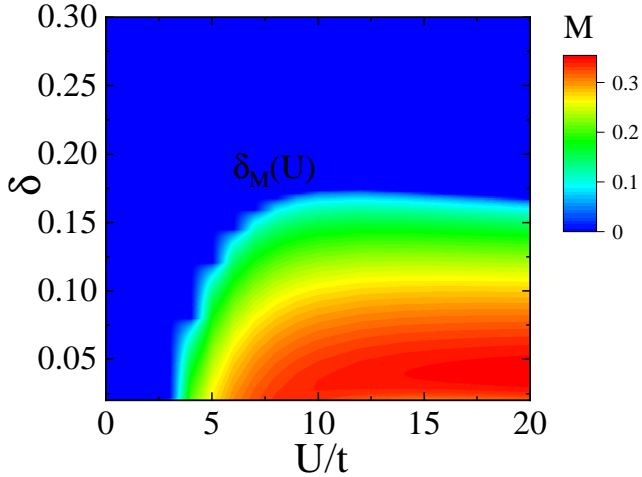


FIG. 8. The staggered magnetization M as function of U and δ obtained by six-site cluster, where $\delta_M(U)$ is the phase boundary between the AFM and PM states.

to that in the square lattice case³⁰. For $U > U_c$, the maximum of Δ_{AFM} occurs at $\delta \sim 0.075$, leading to an interesting vertical re-entrance behavior as δ increases, same as the square lattice case³⁰.

Combining Figs. 8, 9, and 10, a phase diagram in the U - δ plane emerges in Fig. 11. In contrast to the square lattice case³⁰, the crossover U_c in the AFM state at which Δ_{AFM} is maximized, symbolled by the red squares, is shown to be highly δ -dependent. On the other hand, U_c at $\delta = 0$ is smaller than U_{Mott} (red triangle), implying that at half-filling, the coupling strength separating the weak- and strong-coupling regimes is suppressed by long range AFM correlations³⁰. The blue region in this figure enclosed by $\delta_{\kappa}^1(U)$ and $\delta_{\kappa}^2(U)$ is characterized by $M \neq 0$ and $\kappa < 0$ with $\delta_{\kappa}^1(U)$ being the phase boundary between

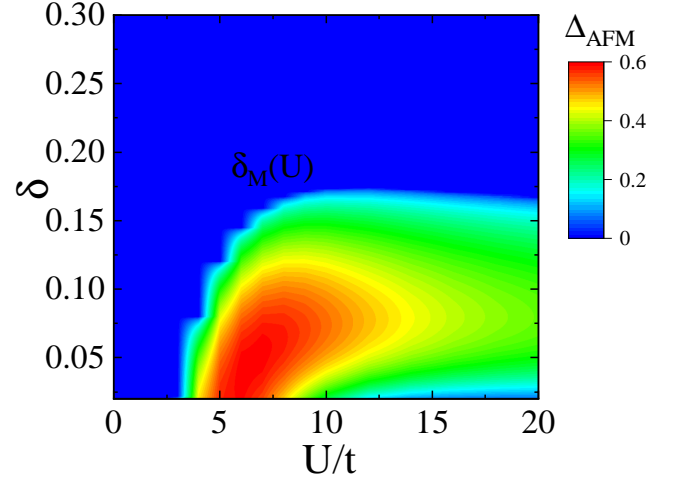


FIG. 9. The AFM gap Δ_{AFM} as function of U and δ obtained by six-site cluster with $\delta_M(U)$ separating the AFM and PM states.

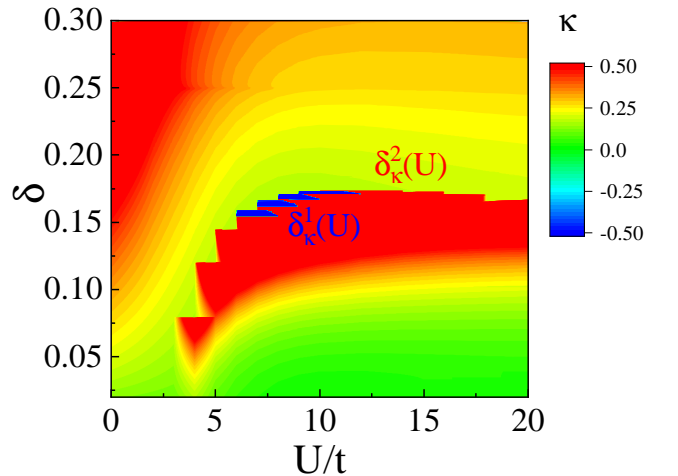


FIG. 10. The compressibility κ as function of U and δ obtained by six-site cluster. The staircase is an artifact because of discrete U 's adopted to calculate κ , i.e., $\Delta U = t$ when $U \leq 10t$ and $\Delta U = 2t$ when $10t < U \leq 20t$, which can only be eliminated in the $\Delta U \rightarrow 0$ limit. The blue region between $\delta_{\kappa}^1(U)$ and $\delta_{\kappa}^2(U)$ is characterized by $\kappa < 0$, where $\delta_{\kappa}^1(U)$ and $\delta_{\kappa}^2(U)$ are delineated by the midpoints of the blue and red steps, respectively. The discontinuities in κ at these two phase boundaries are reflected in the color jumpings.

$M \neq 0$, $\kappa > 0$ and $M \neq 0$, $\kappa < 0$, and $\delta_{\kappa}^2(U)$ between $M \neq 0$, $\kappa < 0$ and $M = 0$, $\kappa > 0$. The region with $\kappa < 0$ is extremely small compared to the square lattice Hubbard model³⁰, and exists only in the vicinity of the phase boundary between the AFM and PM state and at intermediate U .

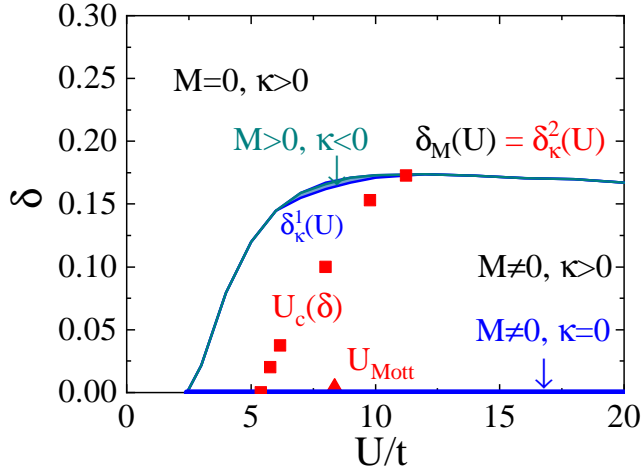


FIG. 11. The U - δ phase diagram of the hexagon lattice Hubbard model within the six-site cluster scheme. The critical coupling $U_{\text{Mott}} = 8.36$ for the Mott transition in the half-filled PM state is marked by the red triangle. The crossover coupling $U_c(\delta)$ in the AFM state at $\delta = 0, 0.02, 0.0375, 0.1, 0.1531$ and 0.1725 are symbolled by red squares, at which Δ_{AFM} reaches its maximum. The half-filling case with $U > 2.43$ is highlighted by the heavy blue line, in which the system is an AFM insulator with $\kappa = 0$.

V. CONCLUSION

We have exploited the cluster slave-spin method to explore extensively the ground state properties of the one-band honeycomb lattice Hubbard model with U and δ as its parameters. At half-filling, the first-order semi-metal to insulator Mott transition in the PM state is revealed, characterized by discontinuities and hystereses in all quantities considered at $U_{\text{Mott}} = 8.36t^{18,21,40}$. In the AFM state, a single direct and continuous phase transition between PM semi-metal and AFMI at $U_{\text{AFM}} = 2.43t$ is substantiated, which belongs to the Gross-Neveu-Yukawa universality class^{9–16,18}, precluding the existence of intermediate phases such as a spin liquid state. At

finite dopings, there exists an extended crossover between the weak- and strong-coupling regimes in the AFM state at which the AFM energy gap Δ_{AFM} reaches its maximum, and the AFM within this crossover is driven by both the kinetic energy and interaction potential gain. The interaction U_c for this crossover is smaller than U_{Mott} at small δ or otherwise when δ is large, which is distinct from the square lattice system where U_c remains almost unchanged with large dopings³⁰.

Moreover, for the half-filled system, by analytically calculating the relation between M and Δ_{AFM} in the vicinity of the PM semi-metal to AFM insulator transition, Eq. (25), we found that to the leading order, M is linearly dependent on Δ_{AFM} , in contrast to the square lattice result that is proportional to $\Delta_{\text{AFM}}(\ln \Delta_{\text{AFM}})^2$ (Ref. 30). This difference is consistent with the vanishing non-interacting DOS at Dirac points in the honeycomb lattice, compared to the van Hove singularity of the free electron DOS at the Fermi surface in a half-filled square lattice.

Finally, an overall phase diagram in the U - δ plane is presented in Fig. 11, the phase boundary $\delta_M(U)$ separating the AFM and PM phases shows a nonmonotonic behavior with the increasing U , which is consistent with the crossover behavior of Δ_{AFM} . The phase boundary between the AFM metal with $\kappa > 0$ and the AFM insulator with $\kappa = 0$ locates exactly at $\delta = 0$. The region with $\kappa < 0$ only exists in the vicinity of the phase boundary between the AFM and PM state and at intermediate coupling strengths, whose area is extremely small compared to the counterpart in the square lattice Hubbard model³⁰.

ACKNOWLEDGMENTS

We thank Shiping Feng, Xiong Fan and Yu Ni for many helpful discussions. This work was supported by NSFC (Nos. 11774033 and 11974049), Beijing Natural Science Foundation (No. 1192011), and the HSCC program of Beijing Normal University.

* txma@bnu.edu.cn

† yjwang@bnu.edu.cn

¹ J. Hubbard, *Proc. R. Soc. Lond. A* **276**, 238 (1963); *Proc. R. Soc. Lond. A* **277**, 237 (1964).

² S. R. White, D. J. Scalapino, R. L. Sugar, E. Y. Loh, J. E. Gubernatis, and R. T. Scalettar, *Phys. Rev. B* **40**, 506 (1989).

³ M. Qin, T. Schäfer, S. Andergassen, P. Corboz, and E. Gull, “The hubbard model: A computational perspective,” (2021), arXiv:2104.00064 [cond-mat.str-el].

⁴ Z. Y. Meng, T. C. Lang, S. Wessel, F. F. Assaad, and A. Muramatsu, *Nature* **464**, 847–851 (2010).

⁵ M. Hohenadler, T. C. Lang, and F. F. Assaad, *Phys. Rev. Lett.* **106**, 100403 (2011).

⁶ M. Hohenadler, T. C. Lang, and F. F. Assaad, *Phys. Rev. Lett.* **109**, 229902 (2012).

⁷ M. Hohenadler, Z. Y. Meng, T. C. Lang, S. Wessel, A. Muramatsu, and F. F. Assaad, *Phys. Rev. B* **85**, 115132 (2012).

⁸ D. Zheng, G.-M. Zhang, and C. Wu, *Phys. Rev. B* **84**, 205121 (2011).

⁹ Y. Otsuka, S. Yunoki, and S. Sorella, *Phys. Rev. X* **6**, 011029 (2016).

¹⁰ M. Raczkowski, R. Peters, T. T. Phùng, N. Takemori, F. F. Assaad, A. Honecker, and J. Vahedi, *Phys. Rev. B* **101**, 125103 (2020).

¹¹ F. F. Assaad and I. F. Herbut, *Phys. Rev. X* **3**, 031010 (2013).

¹² T. Paiva, R. T. Scalettar, W. Zheng, R. R. P. Singh, and J. Oitmaa, *Phys. Rev. B* **72**, 085123 (2005).

¹³ A. Yamada, *International Journal of Modern Physics B* **30**, 1650158 (2016).

¹⁴ S. Sorella and E. Tosatti, *Europhysics Letters (EPL)* **19**, 699 (1992).

¹⁵ S. Sorella, Y. Otsuka, and S. Yunoki, *Scientific Reports* **2** (2012), 10.1038/srep00992.

¹⁶ J. Ostmeyer, E. Berkowitz, S. Krieg, T. A. Lähde, T. Luu, and C. Urbach, *Phys. Rev. B* **102**, 245105 (2020).

¹⁷ J. Ostmeyer, E. Berkowitz, S. Krieg, T. A. Lähde, T. Luu, and C. Urbach, “The antiferromagnetic character of the quantum phase transition in the hubbard model on the honeycomb lattice,” (2021), arXiv:2105.06936 [cond-mat.str-el].

¹⁸ S. R. Hassan and D. Sénéchal, *Phys. Rev. Lett.* **110**, 096402 (2013).

¹⁹ K. Seki and Y. Ohta, “Quantum phase transitions in the honeycomb-lattice hubbard model,” (2012), arXiv:1209.2101 [cond-mat.str-el].

²⁰ A. Liebsch and W. Wu, *Phys. Rev. B* **87**, 205127 (2013).

²¹ Q. Chen, G. H. Booth, S. Sharma, G. Knizia, and G. K.-L. Chan, *Phys. Rev. B* **89**, 165134 (2014).

²² S. Arya, P. V. Sriluckshmy, S. R. Hassan, and A.-M. S. Tremblay, *Phys. Rev. B* **92**, 045111 (2015).

²³ C. Honerkamp, *Phys. Rev. Lett.* **100**, 146404 (2008).

²⁴ S. Raghu, X.-L. Qi, C. Honerkamp, and S.-C. Zhang, *Phys. Rev. Lett.* **100**, 156401 (2008).

²⁵ Y. R. Wang, J. Wu, and M. Franz, *Phys. Rev. B* **47**, 12140 (1993).

²⁶ S. Feng, J. B. Wu, Z. B. Su, and L. Yu, *Phys. Rev. B* **47**, 15192 (1993); S. Feng, Z. B. Su, and L. Yu, *Phys. Rev. B* **49**, 2368 (1994); S. Feng, *Phys. Rev. B* **68**, 184501 (2003); S. Feng, J. Qin, and T. Ma, *Journal of Physics: Condensed Matter* **16**, 343 (2004); S. Feng, Y. Lan, H. Zhao, L. Kuang, L. Qin, and X. Ma, *International Journal of Modern Physics B* **29**, 1530009 (2015).

²⁷ S. R. Hassan and L. de' Medici, *Phys. Rev. B* **81**, 035106 (2010).

²⁸ R. Yu and Q. Si, *Phys. Rev. B* **86**, 085104 (2012).

²⁹ W.-C. Lee and T.-K. Lee, *Phys. Rev. B* **96**, 115114 (2017).

³⁰ M.-H. Zeng, T. Ma, and Y.-J. Wang, “Phase diagram of the hubbard model on a square lattice: A cluster slave-spin study,” (2021), arXiv:2106.05457 [cond-mat.str-el].

³¹ Z.-C. Gu, H.-C. Jiang, D. N. Sheng, H. Yao, L. Balents, and X.-G. Wen, *Phys. Rev. B* **88**, 155112 (2013).

³² W.-S. Wang, Y.-Y. Xiang, Q.-H. Wang, F. Wang, F. Yang, and D.-H. Lee, *Phys. Rev. B* **85**, 035414 (2012).

³³ R. Nandkishore, L. S. Levitov, and A. V. Chubukov, *Nature Physics* **8**, 158 (2012).

³⁴ G. Kotliar and A. E. Ruckenstein, *Phys. Rev. Lett.* **57**, 1362 (1986).

³⁵ T. Ma, L. Zhang, C.-C. Chang, H.-H. Hung, and R. T. Scalettar, *Phys. Rev. Lett.* **120**, 116601 (2018).

³⁶ A. Liebsch and W. Wu, *Phys. Rev. B* **87**, 205127 (2013).

³⁷ N. Bleinstein and R. A. Handelsman, *Asymptotic Expansions of Integrals* (Dover Publications, New York, 1986).

³⁸ T. Ogawa, K. Kanda, and T. Matsubara, *Progress of Theoretical Physics* **53**, 614 (1975).

³⁹ M. Abram, J. Kaczmarczyk, J. Jedrak, and J. Spalek, *Phys. Rev. B* **88**, 094502 (2013).

⁴⁰ M.-T. Tran and K. Kuroki, *Phys. Rev. B* **79**, 125125 (2009).

⁴¹ D. Vollhardt, *Rev. Mod. Phys.* **56**, 99 (1984).

⁴² B.-X. Zheng and G. K.-L. Chan, *Phys. Rev. B* **93**, 035126 (2016).